Experimental Investigation of Mode II Fatigue and Size Effect in Unidirectional Carbon/Epoxy Composite Beams

Adrian Kiuho Lo

A thesis

submitted in partial fulfillment of the

requirements for the degree of

Master of Science in Aeronautics & Astronautics

University of Washington

2023

Reading Committee:

Marco Salviato

Carl Knowlen

Program Authorized to Offer Degree:

Aeronautics & Astronautics

University of Washington

Abstract

Experimental Investigation of Mode II Fatigue and Size Effect in Unidirectional Carbon/Epoxy Composite Beams

Adrian Kiuho Lo

Chair of the Supervisory Committee:
Associate Professor Marco Salviato
Department of Aeronautics & Astronautics

This paper investigates mode II quasibrittle behavior and fatigue characteristics within laminated composite structures and examines these through the lens of size effect. The primary focus of this study is mode II quasi-static fatigue. Employing a closed-molding technique, composite beam specimens of varying dimensions were fabricated in-house, utilizing Toray T800S carbon/epoxy prepregs. An initial pre-crack was deliberately introduced at the midplane of each specimen using a Teflon insert, with predefined crack lengths. An experimental quasi-static fatigue investigation was also conducted using load-controlled tests on geometrically scaled specimens. The results of these fatigue tests enabled the formulation of the threshold and stable crack growth regions of the fatigue Paris Curve for three different specimen sizes. This identified increasing values for threshold Stress Intensity Factors, ΔK_{th}, with increasing specimen size. It also showed increasing slopes for the linear fatigue crack growth for increasing specimen size, demonstrating the size effect influence for both values. The fatigue energy of initiation was also analyzed using both Linear Elastic Fracture Mechanics (LEFM) and Bažant’s Type II Size Effect Law. It was found that calculating these values using LEFM resulted in different values for the smaller specimen sizes, which contradicts the energy of initiation being an intrinsic material property. To address this issue, Bažant’s Type II Size Effect Law was applied to the experimental data which allowed the determination of the fatigue energy of initiation as a consistent material property.

Contents

List of Figures

List of Tables

Acknowledgments

This thesis would not have been possible without the guidance and assistance of my advisor, Dr. Salviato. His experience and valuable advice were imperative throughout each step of my research. I would also like to thank Dr. Carl Knowlen and Dr. Han-Gyu Kim, who both gave me a lot of helpful contributions and feedback during the writing and testing stages. Special thanks goes out to all the members of the MAMS lab, who taught me many things about testing and were always available to answer questions and give feedback. Lastly, I'd like to thank all my friends and family for their unwavering support through this process.

1. Introduction

1.1. Overview of Composite Materials

Composites are materials that are widely used in the aviation and space industries due to their excellent physical and mechanical properties. They are essentially a combination of two or more materials with different physical and chemical properties, which when combined create a material with superior properties compared to the individual components. In most cases, composites consist of a stiff fiber component placed within a softer component called a matrix[5]. The most common types of aerospace composites include carbon fiber, glass fiber, and ceramic matrix composites.

One of the primary reasons for the popularity of aerospace composites is their high strength-to-weight ratio. This is particularly important in the aerospace industry, where weight reduction is critical for achieving higher performance, fuel efficiency, and payload capacity. Aerospace composites are also known for their excellent resistance to corrosion and impact, making them an ideal choice for aerospace applications[6].

The use of aerospace composites has revolutionized the aviation industry by enabling the design of aircraft with unique properties that would have been impossible with traditional materials such as metals. Aerospace composites are used in various aircraft components, such as wings, fuselage, and engine parts. They are also used in space applications, such as satellites, spacecraft, and launch vehicles. Another advantage that composites have is the relative ease of design. Because of the way composites are created, composite materials can generally be formed into much more complex shapes than traditional metals can, allowing for more flexibility in the design stage.

Despite the many advantages of aerospace composites, their use also presents some challenges. One of the most significant challenges is their high cost, which is due to the complex manufacturing processes and the high cost of raw materials[5]. Additionally, the use of composites requires specialized manufacturing techniques, which can be time-consuming and require highly skilled personnel. As such, the manufacturing of aerospace composites requires a significant investment in terms of time, resources, and expertise. However, the benefits of using composites in aerospace applications are far-reaching, making the investment worthwhile.

The development of composite materials has significantly impacted the aviation industry, with aircraft such as the F-35 and Boeing's 787 utilizing a large percentage of composite materials by weight[7, 8]. However, as aircraft technology continues to evolve, faster and more agile aircraft such as hypersonic flight vehicles are being introduced. Due to the higher flight speed, the material experiences greater stresses than in typical subsonic and supersonic flight, causing very high stresses in structures like aircraft skin panels causing a premature failure in the material, usually through thermal or mechanical buckling[9]. An example of this can be seen in Figure 3, where the wrinkles are caused by aerodynamic loading from flight conditions. The non-linear material behavior that occurs due to in-flight loading can lead to low-cycle fatigue failure. Due to the nature of the material response, these loads are often more affected by mode II failure, which is a shearing failure, rather than the more prominent mode I failure[10].

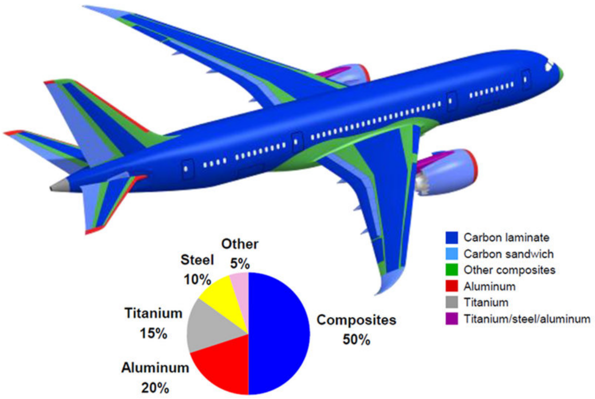

(a) Boeing 787 Dreamliner, 50% composite material by weight[11]

(b) US Air Force F-35, 35% composite material by weight[7]

Fig. 1 Examples of Aircraft using Composite Materials

1.2. Theory

In this research, the investigation on Mode II failure was continued on unidirectional carbon/epoxy specimens. Carbon/epoxy structures as well as composites in general, exhibit quasibrittle behaviors. This indicates a large fracture process zone(FPZ) which experiences progressive softening damage until it fractures[12, 13]. Due to the quasibrittle nature of these materials, Linear Elastic Fracture Mechanics cannot be used. Instead, quasibrittle structure's characteristics are dependant on the size of the structure[12, 13].

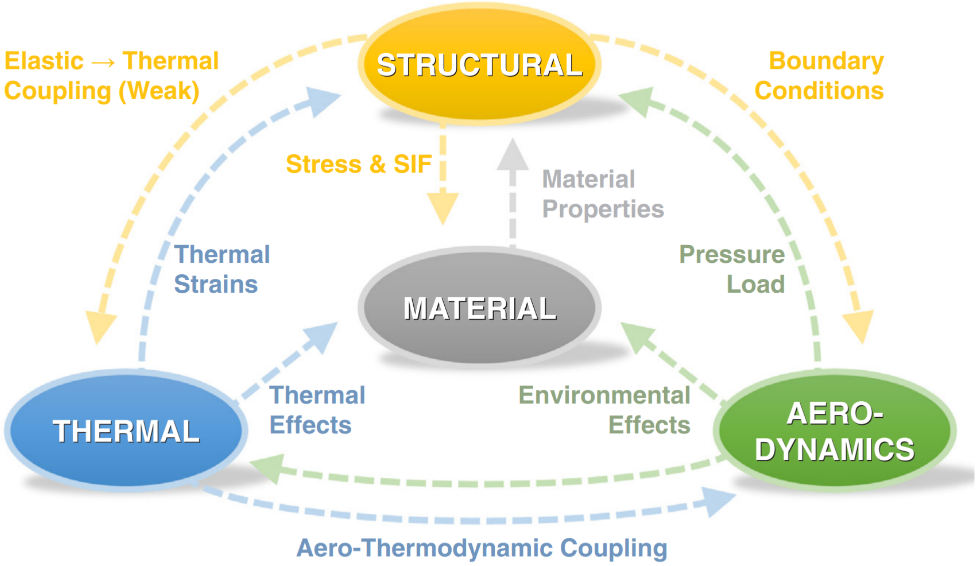

Fig. 2 Map showing connection between aerodynamic, structural and thermal effects[1]

1.2.1. Size Effect

There are three different kinds of fracture mechanics, each used for different situations. The first is LEFM, which is the mechanics of perfectly brittle fracture. The second kind is elastoplactic or cohesive fracture mechanics, which generally applies to non fatigued metals and plastics. The third kind is quasibrittle fracture mechanics or the cohesive softening fracture mechanics. Quasibrittle materials are generally heterogeneous with brittle components. At a large scale, every quasibrittle structure, become perfectly brittle. However, when the structure is small enough, the structures begin to demonstrate quasibrittle behavior[13]. As the size increases, the response of the material transitions from ductile to brittle and is the source of the quasibrittle size effect. Size effect can be broken down into two types. The first applies to structures without any notches or discontinuities, while the second applies to those with notches or preexisting cracks. For this research, only type II size effect will be examined. When a structure is not much larger than the size of the FPZ, the failure will be quasiplastic. For a type II structure, Bažant's Size Effect Law is shown below in Equation 1[13].

$$\sigma_N = B f_t (1 - \frac{D}{D_0})^{-1/2} \tag{1}$$

In this, B is a dimensionless parameter, f_t is the material toughness, D is the characteristic length of a geometrically scaled structure, and D_0 is the transitional size. This equation can be rearranged in terms of material characteristics, as shown in Equation 2[13].

$$\sigma_N = \sqrt{\frac{E' * G_f}{g_0' c_f + g_0 D}} \tag{2}$$

Fig. 3 Effects of aerodynamic loads on constrained skin panels

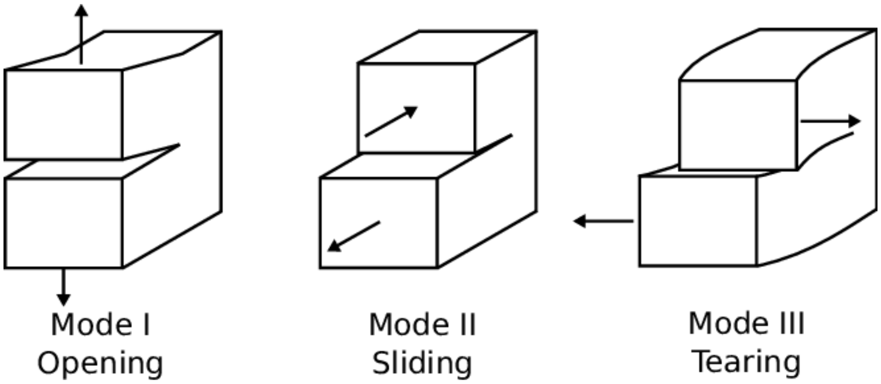

Fig. 4 Three modes of fracture

Where E’ is the material modulus of elasticity, G_f is the material fracture energy, c_f is the effective FPZ size, D is the characteristic length of the structure, g is the dimensionless energy release rate, and g' is its derivative. Both g and g' are dependant on the crack length. Figure 5 depicts Bažant’s Size Effect Law as well as its deviation LEFM on a log-log scale of the nominal stress versus the structure size.

1.2.2. J-integral

Another fundamental concept of fracture mechanics is the J-integral. This integral was was able to show that contour line integral taken around a crack or notch tip, was independent of the path taken[13]. By calculating the change of work to the crack tip. The work done is separated into two different sources, the work done by the strain energy and the

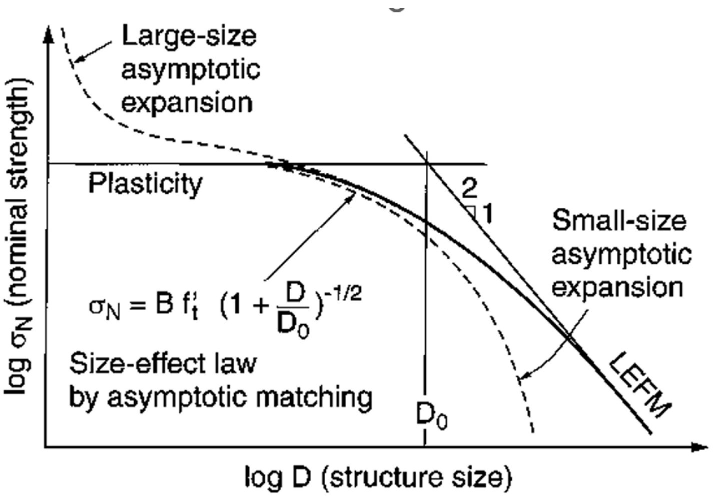

Fig. 5 Bažant's Size Effect Law, showing deviation from LEFM[2]

work done by the traction force. The change in work can be written in the form of equation 3.

$$\Delta W = -[\int_\Gamma (t_i \delta u_i) ds - \int_\Gamma \bar{U} \delta a dx_2] \tag{3}$$

Where δa is the change in crack length, $\bar{U}\delta a dx_2$ is the strain energy and $t_i \delta u_i$ is the work that the traction exerts. In this case, Γ is any path or volume that surrounds the crack tip. Examples of these paths are shown in Figure 6. Since the J-integral is also defined as

$$J = \lim_{\delta a \to 0} \frac{\delta W}{\delta a} \tag{4}$$

Equations 3 and 4 can be combined into Rice's J-integral.

$$J = \int_\Gamma (\bar{U} dx_2 - \sigma_{ij} n_j u_{i,1} ds) \tag{5}$$

The main importance of the J-integral is that it is equal to energy release rate, G, calculated through LEFM in certain circumstances. This is true if and only if, the non-elastic zone can be reduced to a singular point within the contour, the faces of the notches are not subject to any traction, and that the crack is planar[13]. The J-integral can also be used in cases where the elasticity is nonlinear, and can be used to characterize the yielding zone of both linear and non-linear elastic materials.

1.2.3. Traction Separation Law

Using LEFM, is generally assumed that there is a point of infinite stress at a sharp crack tip, leading to a stress singularity in the near tip stress field[14]. This means that in order to characterize the stresses at the crack tip, other

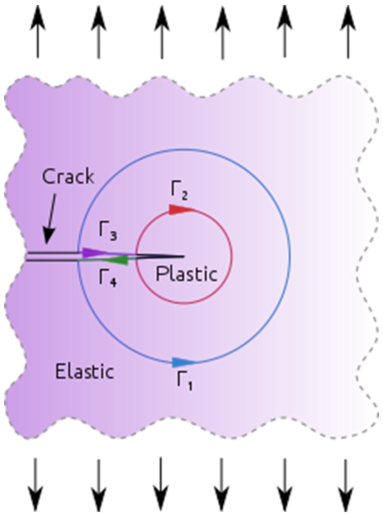

Fig. 6 Paths for J-integral around a crack tip

techniques must be applies. The cohesive crack model allows the description of the fracturing process without the inclusion of the stress singularity. This model introduces two surfaces which are able to transfer stresses from one another. Figure 7a shows these traction forces as the crack separates. As these surfaces separate due to crack propagation, the traction forces experienced will increase until a maximum, then trend to zero. The main takeaway from the cohesive crack model is the introduction of the traction separation law. This law describes the constitutive behavior of the two cohesive surfaces by comparing the traction force experienced to the relative displacements of the surface. This is considered a material property and shows the evolution of the cohesive stresses in the Fracture Process Zone.

The traction-separation law generally must be derived through experimental results. The simplest is to just employ a linear softening model. This law can be adjusted to fit experimental results by picking a different softening model as seen in Figure 7b. Certain materials may require bi-linear or tri-linear models, while others may even need exponential or parabolic models to capture their behavior[14].

1.2.4. Fatigue

To achieve this, researchers and engineers have developed various models and laws that describe the relationship between the number of cycles to failure (N) and the applied stress or strain amplitude. Among these, the Paris-Erdogan Law, is one of the most widely used and influential fatigue crack growth models[15–17].

The Paris Law describes the relationship between crack growth rate and stress intensity factor range over a wide range of cyclic loading conditions. It suggests that the fatigue crack growth rate increases with higher stress intensity factor ranges. The exponent m plays a significant role in characterizing the material's sensitivity to cyclic loading, providing valuable information about its resistance to fatigue.

When plotting the Paris Law equation, a log-log scale is typically used. This results in a straight line known as the

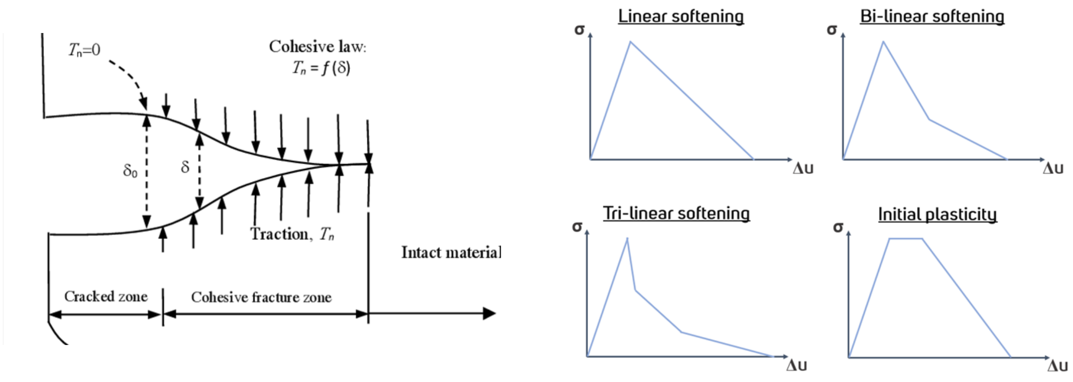

(a) Cohesive zone model, with traction forces[2]

(b) Examples of different Traction Separation Laws

Fig. 7 Cohesive Zone model and the Traction Separation Law

Paris Law curve. A diagram of an example of the Paris Law curve can be seen in Figure 8

The important parts of the Paris Law curve are as follows:

Region A: In this region, characterized by relatively low stress intensity factor ranges, the crack growth rate is minimal and almost constant. During this stage, crack propagation is negligible, and the material is relatively resistant to fatigue failure.

Region B: As the stress intensity factor range increases, the crack growth rate rises significantly, indicating a more rapid propagation of the fatigue crack. It is in this phase that the Paris-Erdogan Law becomes more applicable, and the exponential relationship between crack growth rate and stress intensity factor range becomes evident.

Region C: In the final region, the stress intensity factor reaches its critical point. This phase is usually defined by unstable crack growth and dynamic failure[17].

The Paris Law is of paramount importance in fatigue testing and engineering design. Its ability to quantitatively describe the crack growth behavior in materials under cyclic loading allows engineers to predict the fatigue life of components accurately. By understanding how cracks propagate and assessing the material's sensitivity to cyclic loading, the Paris Law aids in enhancing the reliability, safety, and performance of critical structures in industries such as aerospace, automotive, and civil engineering.

1.3. Previous Work

1.3.1. End Notched Flexure Testing Methods

Three methods of testing mode II fractures was researched by Shivakumar et al. End notched flexure (ENF), a modified Japanese International Standard (JIS) and ASTM D7905M-14 were tested on unidirectional carbon/epoxy composites to compare the testing methods. The differences of these test methods are highlighted in Figure 9. Figure 9a shows the ENF method, while Figure 9b and 9c shows the original JIS and the modified JIS respectively. In addition,

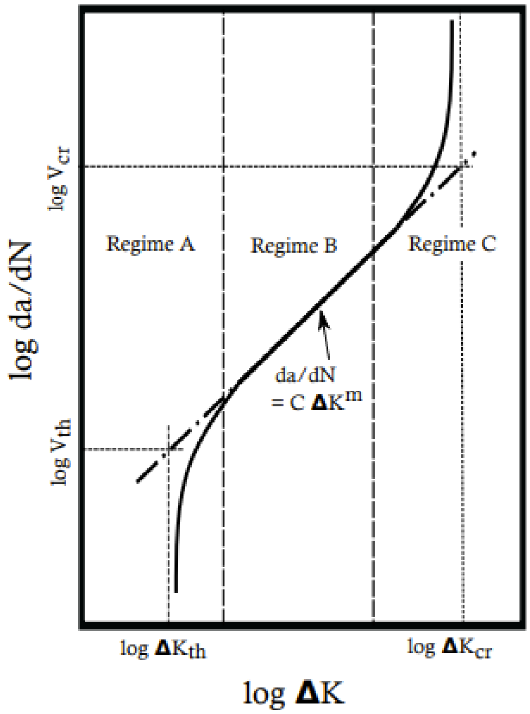

Fig. 8 Example of a Paris Law Curve

this looked to explore the differences between non-precracked(NPC) and precracked(NC) specimens for the ASTM standard, which refer to Figure 9d and 9e, respectively. All three use an ENF specimen undergoing a three point loading test, but have different methods to calculate G_{IIc}. Each method also has a different way to manufacture the crack tip for the non-precracked case. For ENF, the crack is created with 12.7 μm thick FEP or Teflon. The modified JIS uses a PTFE coated steel rod of diameter $0.25mm$, in place of the original JIS which uses a PTFE strip. For the ASTM, a teflon insert is used. The specimens used in this study was a 20-ply AS4/8552 prepreg from Hexcel Composites. A fracture test was then conducted for each of the three methods. It was found that for the JIS method, up to 5% of the total G_c was due to the presence of the mode I stress state, which meant that the G_{IIC} would always be lower than those from the ENF and ASTM methods. Through the ASTM test, it was found that precracking has a large effect on the fracture toughness, finding that the PC case had a 26% lower fracture toughness than the NPC case[3]. This highlights the differences between the NPC and PC specimens. The NPC specimens will use the teflon inserts and will have a blunt crack, while the PC specimens will have a sharp crack tip, created by a fracture test of an NPC specimen, as specified in ASTM D7905[18]. The creation of the sharp crack tip requires a compliance calibration test to be done in order to identify the location of the new crack tip. This also can cause issues with testing PC specimens. Due to the fracture test being done already, micro-fractures can already exist before the any test is done on the PC specimen. This can cause varied results and inconsistencies when compared to that of the NPC specimens. In order to ensure consistent

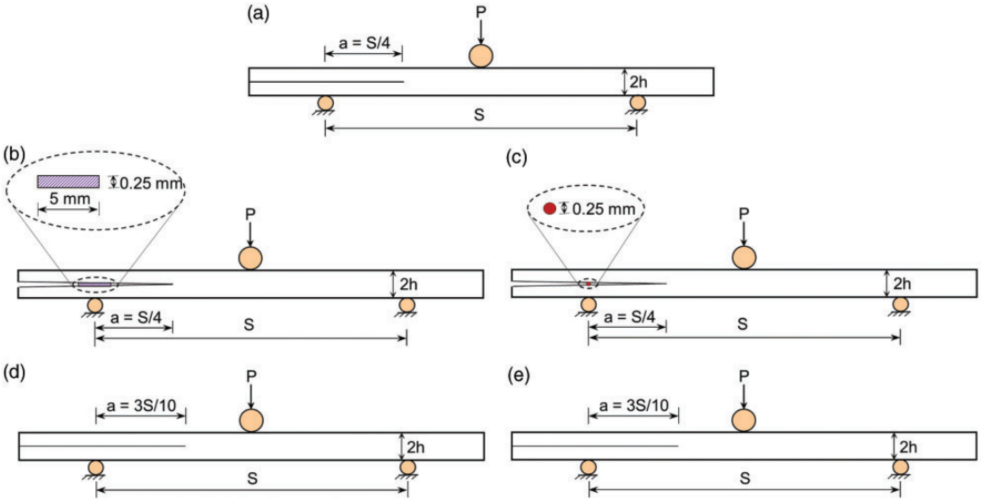

Fig. 9 ENF testing methods investigated by Shivakumar et al.[3]

results across tests, NPC specimens will be used in this research.

1.3.2. Mode II size effect

A study was conducted by Salviato et al. in order to observe the size effect on mode II fracture in laminated composites. The experiments were conducted on a DGEBA-based epoxy resin with a twill 2x2 carbon layup. The ENF specimens used were geometrically scaled with a 2:3:5 scaling method, except for the width, which remained constant throughout the tests.

Due to the appearance of micro-damage in the specimens, the size of the FPZ in front of the crack tip is non-negligible for the smaller specimen size. Size effect testing was used in order to circumvent the issues caused by standard testing procedures, such as snap-back instability. Bažant Size Effect Law, shown in Equation 2, was used to analyze the fracture tests on the specimens. The results of the fracture test in Figure 10 show normalized strength versus normalized characteristic thickness in a log-log plot. From a linear regression of the data, it was found that the fracture energy was 2.25 N/mm and the equivalent FPZ length was 33.51 mm[19]. Theses result show a good fit with the size effect law due to the scaling of the characteristic length. Using LEFM to estimate these same values yields various fracture energies for various sizes, which contradicts the assumption that the fracture energy is a material property.

A finite element analysis of the experiments was also conducted using a cohesive zone model. A linear mode II traction separation law was used to verify the results, which found an agreement between the FEA and the experimental results. It was stated that the use of a bilinear traction separation law would likely lead to the model being able to predict the snap-back instability. These results were able to validate the size effect law proposed by Bažant and identified the shortcomings of LEFM, and that the size effect law should be used in computational models[19].

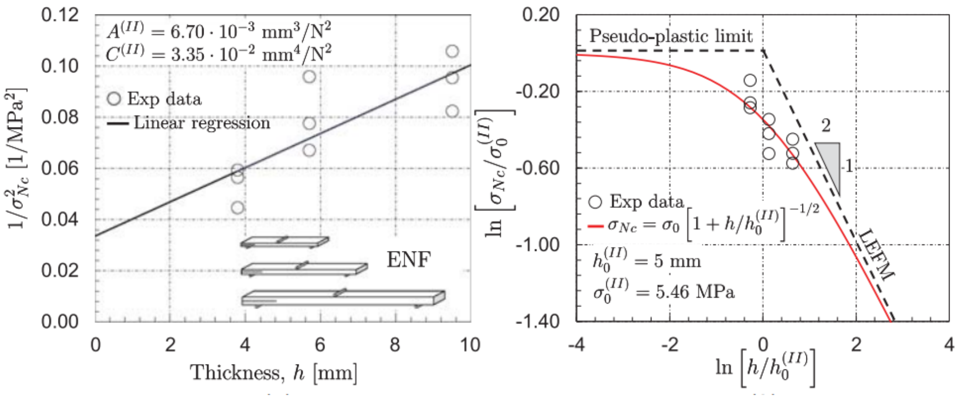

Fig. 10 Linear Regression and Size effect plot from ENF fracture tests of Salviato et al.

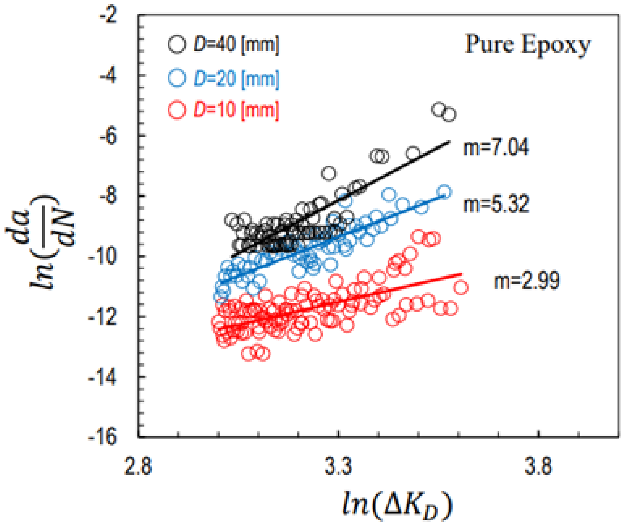

Fig. 11 Paris-Erdogan curves from fatigue testing done by Guo et al.

1.3.3. Paris Law

An investigation on the scaling of fatigue crack growth was done by Guo et al[20]. This was done by observing the size effect on the Paris-Erdogan law, which relates the stress intensity factor with crack propagation rate. A single edge notch bending test was used to test geometrically scaled pure epoxy specimens. Because of the transparency of the materials, the crack growth propagation was monitored via a digital microscope. Through this study it was found that there was a noticeable size effect on the coefficients of the Paris-Erdogan law under the cyclic loading conditions, which was not the case for pristine epoxy under quasi-static loading conditions[20]. The resulting Paris-Erdogan curves are shown in Figure 11. The tests performed were Single-Edge Notched Bending test, which focus on Mode I fracture. However, very little is currently known about size affected fatigue, so these results can still be used to highlight the importance of accounting for the effects of FPZ in fatigue crack growth models.

1.4. Goals and Motivation of Thesis

Mode I fractures and failures in quasibrittle materials has be thoroughly researched in the past[19–21]. In contrast, investigations into mode II fractures have been relatively scarce. Only recently has a standardized test method for End-Notched Flexure (ENF) specimens been adopted, enabling the study of fracture energy associated with mode II fractures. Given the stress amplitudes experienced during in-flight loading, specifically in supersonic and hypersonic flight regimes, a comprehensive exploration of these mode II material properties and crack propagation mechanisms must be done. This research focuses on an important gap in our understanding by incorporating fatigue behavior in mode II size effect testing. Fatigue, a phenomenon involving the progressive weakening of materials under cyclic loading, plays a critical role in the structural integrity of materials subjected to dynamic stresses. Furthermore, fatigue in composites is a topic that is very commonly overlooked because of the common misconception that composite materials do not fatigue. In fact, when undergoing fatigue, delaminations may occur, which progressively reduces the stiffness and strength of the material, and will eventually result in failure of the structure. Therefore, understanding cyclic delamination growth is essential for the application of composites to high performance structures, such as aircraft. Investigating the interplay between mode II fractures and fatigue enhances the applicability of the findings to real-world scenarios, thereby broadening the scope of this study's implications. To accomplish this, first, a fatigue study of three different specimen sizes will be conducted to construct a Paris-Erdogan curve for carbon/epoxy beams using the Toray T800s material. Then, size effect testing will be conducted on the same three sizes of specimen to observe the deviation of LEFM and the correlation to the Size effect law.

2. Manufacturing

The research paper focuses on investigating the fatigue life of carbon composite ENF beams. The specimens were manufactured in-house at the University of Washington's Mechanical Engineering composite shop, following the typical prepreg carbon plate layup process outlined in ASTM D5687[22]. Using carbon prepreg, a predetermined number of plies were laid up to achieve the desired specimen thickness. These layups were then baked in an autoclave to cure, after which specimens were cut and dimensioned. The specimens were made of Toray T800S-24K material with 160 gsm and 35% resin content and dimensioned according to the geometry outlined in ASTM D7905[18]. In order to properly scale the specimens for size effect testing, a scaling law was created to obtain measurements for a new geometry based on a scaled specimen thickness. A thin Teflon insert was used, as specified in the ASTM Standard D7905, which allows for a maximum allowable Teflon thickness of 0.0005 in (12.7 µm) in mode II fracture of ENF specimens[18].

2.1. Manufacturing Process

The process of manufacturing carbon plates at UW using the in-house closed molding technique is the same for all of the specimens. Prepreg material is kept in an industrial freezer to prevent precuring and lengthen shelf-life, but must

Size	Target Width(mm)	Target Thickness(mm)	Actual Width(mm)	Actual Thickness(mm)	Number of Plies
1	25	1.2	25.68	1.48	10
2	25	2.4	24.63	2.78	18
3	25	4.8	25.23	5.42	34

Table 1 T800S Fatigue Specimen Dimensions

be thawed before use by exposing it to a fan for 1-2 hours at ambient temperature. Once thawed, the prepreg material is cut into predetermined plate sizes using a CNC fabric cutter and laid up onto a metal plate using the material sandwich method. After every 8-10 plies, a debulking period under vacuum removes any voids present in the layup over a period of at least an hour, which supplies pressure on all sides of the layup. A Teflon insert is placed in a predesigned position at the midplane to ensure the final specimens have the necessary crack length. The ply stacking continues until the desired thickness is achieved. The appropriate autoclave bake cycle using the proper pressure and temperature was done according to the manufacturer's instructions. After the autoclave bake, the plates are cut using an in-house tile saw to create carbon beams with the desired geometry[4]. The dimensions of each beam are precisely measured using calipers at small intervals along each beam, as specified by ASTM D7905. The number of plies used for each size and the specimen dimensions are listed in Table 1. As can be seen, the thickness values were greater than the target thickness, likely due to the relatively high fiber percentage leading to a slightly thicker ply. An image of each step in the manufacturing process can be seen in Figure 12.

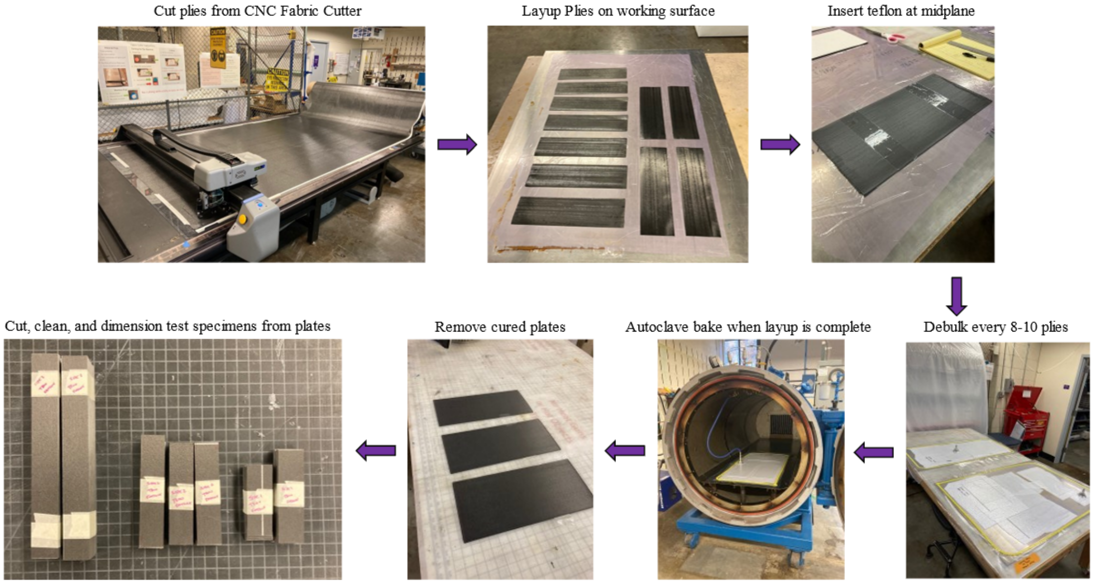

Fig. 12 Manufacturing Process for ENF specimens[4]

3. Mode II Fatigue of ENF Specimens

3.1. Experimental Setup

ENF specimens were tested on the Psylotech micro-load frame in Guggenheim Hall 114. The purpose of the tests was to evaluate both quasi-static compliance and cyclic fatigue behavior of the specimens.

To maintain consistency in compliance data, the testing setup remained the same for both the quasi-static compliance test as well as the fatigue tests. This involved using a scaled span length and initial crack length specific to the size of the specimen. The loading and support rollers used in the frame adhered to the quasi-static ENF standard test method, with diameters of 3.04 mm and 3.10 mm for size 1 and 2, respectively, and with diameters of 4.76 mm and 4.78 mm for size 3. The testing set up example for the size 2 specimen's 3-point bend test can be seen in Figure 13.

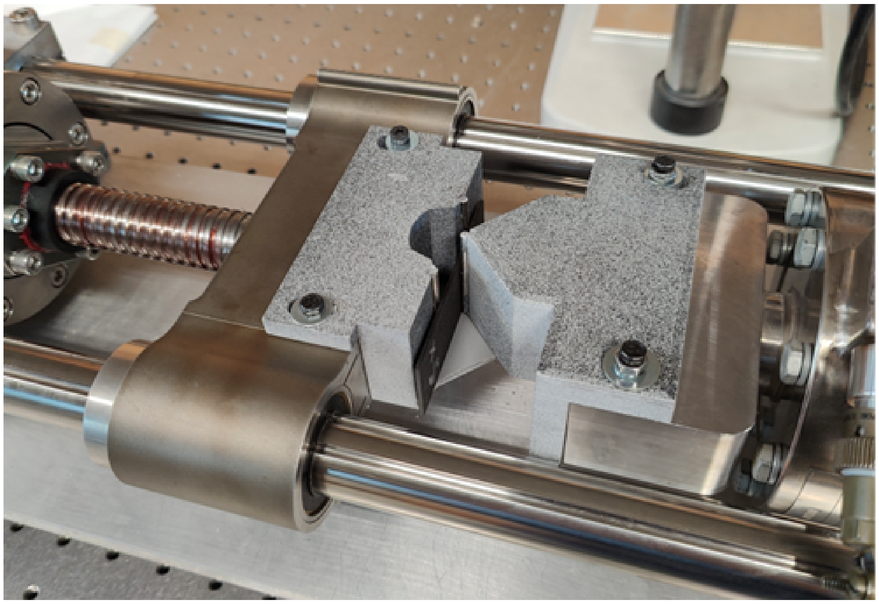

Fig. 13 Size 2 3-point bend fatigue test setup

The testing setup included a computer interface and mechanical controls coupled with a 10 kN load cell. These controls allowed the input of test parameters to define the tests, specifying target amplitudes, frequency, data sampling rates, and the number of cycles. An example of the interface setup can be seen in Figure 14. From this menu, it is also possible to change the control type as well as the loading type. The current force and displacement are also displayed on screen.

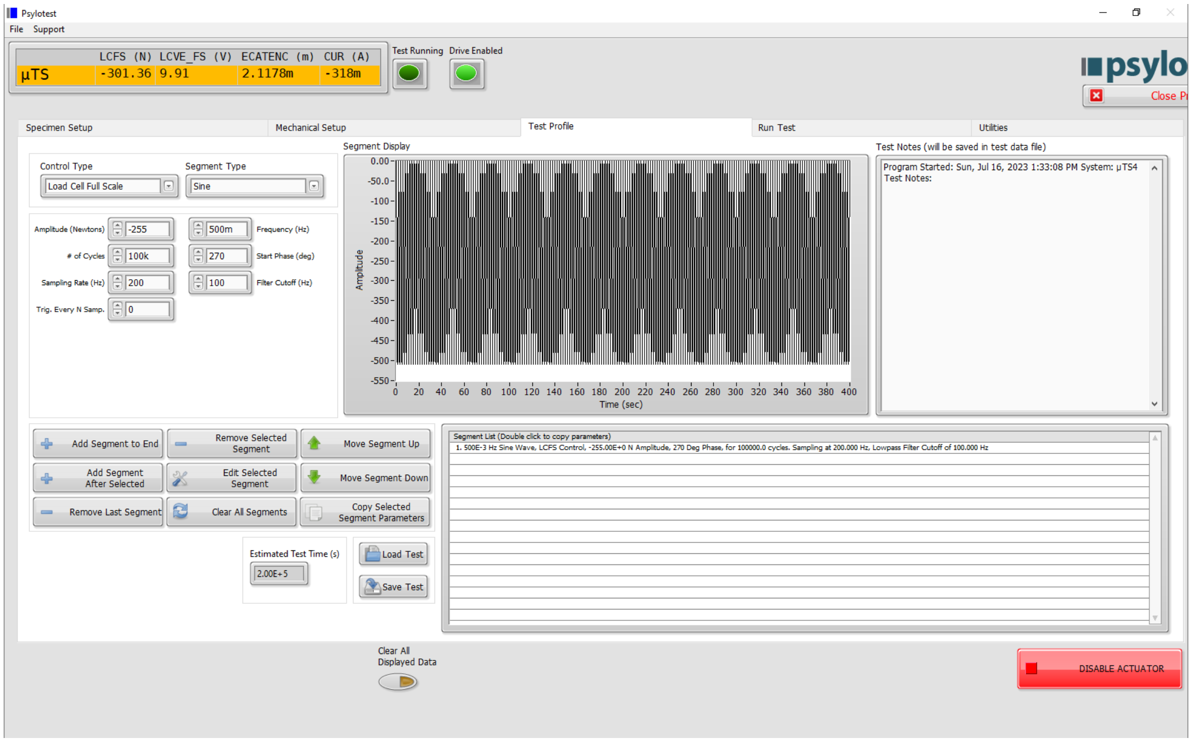

	LCFS (N)	LCVE_FS (V)	ECATENC (m)	CUR (A)
µTS	-301.36	9.91	2.1178m	-318m

Control Type: Load Cell Full Scale
Segment Type: Sine
Amplitude (Newtons): -255
Frequency (Hz): 500m
# of Cycles: 100k
Start Phase (deg): 270
Sampling Rate (Hz): 200
Filter Cutoff (Hz): 100
Trig. Every N Samp.: 0
Estimated Test Time (s): 2.00E+5

Test Notes (will be saved in test data file)
Program Started: Sun, Jul 16, 2023 1:33:08 PM System: µTS4
Test Notes:

Segment List (Double click to copy parameters)
1. 500E-3 Hz Sine Wave, LCFS Control, -255.00E+0 N Amplitude, 270 Deg Phase, for 100000.0 cycles. Sampling at 200.000 Hz, Lowpass Filter Cutoff of 100.000 Hz

Fig. 14 Psylotech Load Frame Computer Interface

This test setup allowed for two different types of fatigues testing: displacement control and load control. In displacement controlled tests, the load amplitude decreased as the specimen compliance increased due to crack growth. This approach allowed for constructing the Paris Law curve from right to left, eventually reaching the region of infinite life where no further crack growth occurs at a fixed displacement. On the other hand, load controlled tests involved increasing the displacement amplitude as the specimen compliance changed, approaching the right hand in the Paris Law curve, which represents rapid crack growth[17].

Since this testing is a continuation of an previous investigation, this experiment was only focused on the load controlled tests of size 1-3 T800 composite specimens.

Currently, no test standard exists for ENF specimens undergoing fatigue in mode II conditions. Because of this, the quasi-static test method, ASTM D7905, was used as a basis to perform these fatigue tests. A similar method to that used by Al-khudairi et al. was applied to this research[23].

3.2. Results and Analysis

The primary objective of this research was to establish a Paris Law curve that governs the fatigue crack growth in three differently sized specimens. This investigation can be broken down into a series of steps. Firstly, the compliance calibration test results were determined, which were then used for further calculations. Next, the calculation of crack length and compliance over the total number of cycles was plotted. Finally, the previous two steps were combined to

Size	a_1(mm)	a_0(mm)	a_2(mm)
1	7	10	13
2	15	20	25
3	30	40	50

Table 2 Crack Lengths for Compliance Calibration

Size	Average Fracture Load(N)
1	644.16
2	930.96
3	1346.44

Table 3 Average Fracture Loads for Size 1-3 Specimens

facilitate construction of the Paris Law curves.

3.2.1. Compliance Calibration

For each specimen, three compliance calibration tests were performed at predetermined crack lengths shown in Table 2. Due to previous research on this topic, the average fracture loads for each specimen have been recorded and are shown in in Table 3. Using these values, the target compliance loading values can be calculated through the following equation.

$$P_{cc} = P_{cr} \frac{a_0}{a_c c} \tag{6}$$

Following the procedure from ASTM Standard D7905, the peak forces during the compliance calibration should be equal to 50% of the expected force(P_{cc})[18]. This gives us all the expected compliance calibration loading values, shown in Table 4

These compliance calibration tests must be completed before conducting fatigue testing in order to properly determine the specimen compliance at each crack length. This compliance data is then used in a linear regression analysis to determine compliance values specific to each beam, denoted as A and m. These values are then used to calculate beam compliance and the change in Stress intensity factor, ΔK, to construct the Paris Law curve. The linear regression

Size	P_{CC}(N)		
	a_1	a_0	a_2
1	460.11	322.08	247.75
2	620.64	465.48	372.38
3	897.62	673.22	538.57

Table 4 Compliance Loading Values for Size 1-3 Specimens at each crack length

equation takes the form of Equation 7

$$C = A + ma^3 \tag{7}$$

where C represents the specimen compliance and a represents the crack length. An example of the compliance load displacement plots as well as the linear regression are shown below in Figures 15 and 16

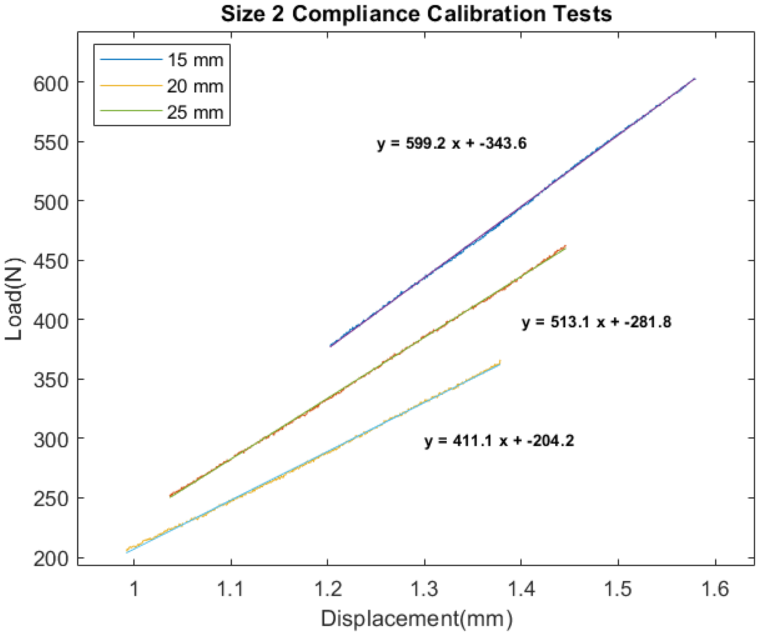

Fig. 15 Size 2 Compliance Calibration Tests

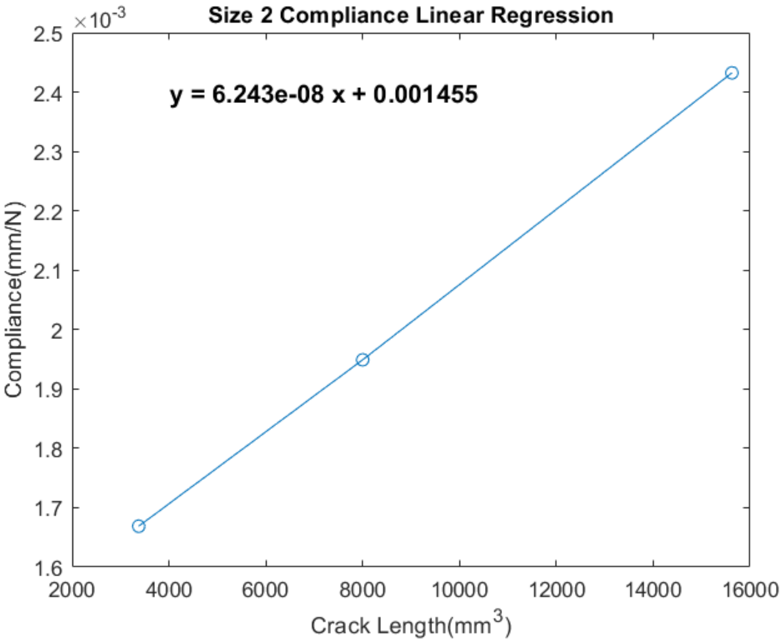

Fig. 16 Size 2 Compliance Calibration Linear Regression

Using the compliance values from above, the crack length and compliance can then be calculated during each cycle using the experimental data. Rearranging equation 7 allows us to solve for the crack length for each cycle, as seen in Equation 8

$$a_n = \left(\frac{C_n - A}{m}\right)^{\frac{1}{3}} \tag{8}$$

The compliance for each cycle, C_n, can be found based on the difference between the max and min load or displacement, shown in Equation 9. The difference used for the calculation depends on the control type for that test. An example of how the compliance is calculated is shown in Figure 17.

$$C_n = \frac{d_{max} - d_{min}}{P_{max} - P_{min}} \tag{9}$$

The maximum and minimums are found from the sinusoidal data of the load or displacement curves of each test. For load control tests, the values of P_{max} and P_{min} should stay constant throughout the test. The opposite is true for displacement control, where the values of d_{max} and d_{min} are constant. All the tests in this research are load controlled, so the difference in displacement is what will be used to calculate compliance. Examples of the Displacement vs cycle number are shown in Figure 18 Since the compliance calculations are heavily based on the differences in local maxima and minima, its important to have a high data sampling rate in order to capture the true peaks of the sinusoidal data.

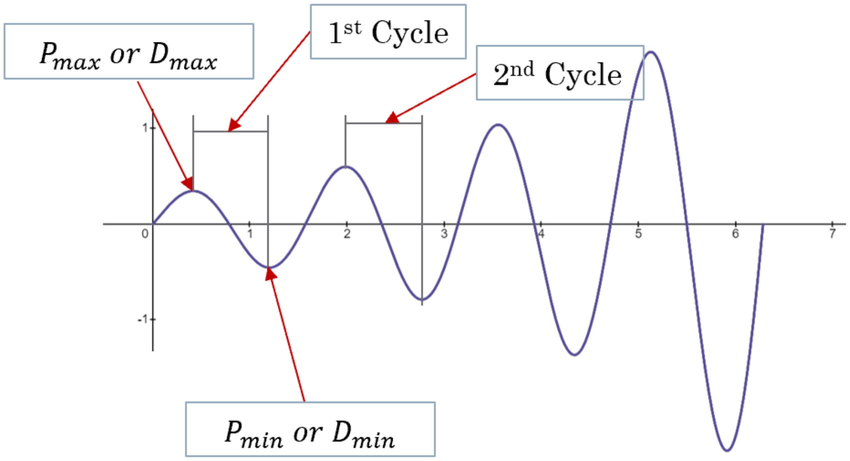

Fig. 17 Example of method to calculate compliance

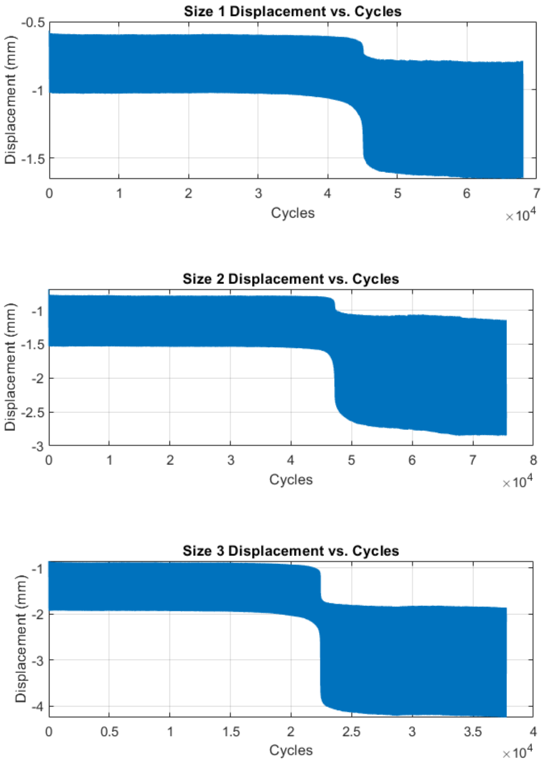

Fig. 18 Size 1-3 Experimental Results for Load Controlled Test

Using the experimental results in Figure 18 with Equations 8 and 9, the crack length and compliance can be calculated for each cycle during the testing. These can be seen in Figures 19, 20, and 21.

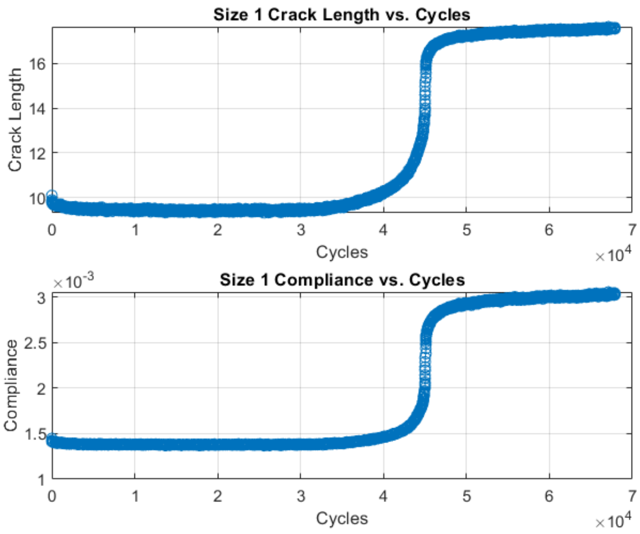

Fig. 19 Size 1 Compliance Calibration Linear Regression

3.2.2. Paris Curves

According to Paris Law, it was shown that there is a correlation between the rate of crack growth, $\frac{da}{dN}$, and the variation of the stress intensity factor, ΔK, in the form of a power law, as shown in Equation 10

$$\frac{da}{dN} = C\Delta K_{II}^{m} \tag{10}$$

By using the crack length data as a function of the number of cycles, values for $\frac{da}{dN}$ can be calculated. By focusing on the section of the data where there is crack growth, a 9th order polynomial was used to provide the best correlation with the data. An example of this fit equation for the size 3 specimen can be seen in Figure 22

Then, using the polynomials, the derivative of the polynomial can be taken with respect to the cycle number. This will provide the rate of change of the crack growth vs. the number of cycles.

To calculate the value of K_{II}, one of the fundamental equations of LEFM is used to relate the stress intensity factor with the energy release rate, G_{II}, in Equation 11

$$K_{II} = \sqrt{EG_{II}} \tag{11}$$

Following this the energy release rate can be calculated through Irwin's Energy approach. The energy release rate is defined as the loss of total potential energy, Π, per unit area swept by the crack growth, denoted by A, as shown in Equation 12

$$G = \frac{d\Pi}{dA} \tag{12}$$

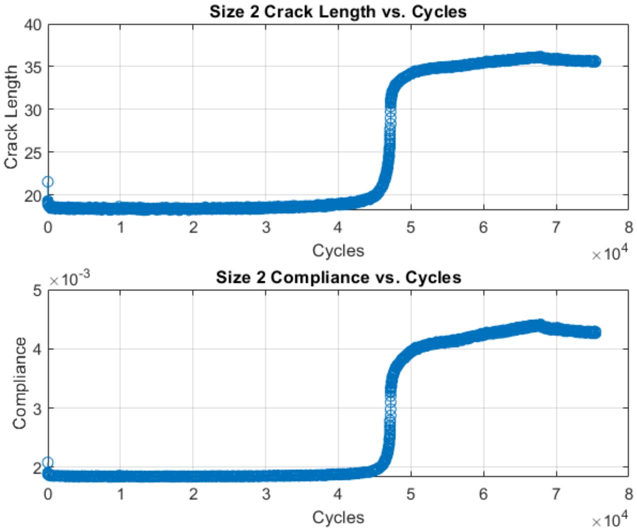

Fig. 20 Size 2 Compliance Calibration Linear Regression

Since these tests are load controlled, the total potential energy can be defined as

$$\Pi = U - W \tag{13}$$

Where U is the stored elastic strain energy and W is the external work done on the beam. These two values can also be defined as shown in Equations 14 and 15

$$W = P\delta \tag{14}$$

$$U = \int_0^{\delta} P d\delta = \frac{P\delta}{2} \tag{15}$$

Where P is the applied load and δ is the deformation of the beam. Substituting Equations 14 and 15 into Equation 12 yields 16

$$G = \frac{1}{b}(\frac{\mathrm{d}U}{\mathrm{d}a})_P \tag{16}$$

Now, the compliance can also be defined as a ratio of the deformation to the applied load, shown below

$$C = \frac{\delta}{P} \tag{17}$$

Substituting this into 15 and plugging that into 16 gives Equation 18

$$G = \frac{P^2}{2b}\frac{\mathrm{d}C}{\mathrm{d}a} \tag{18}$$

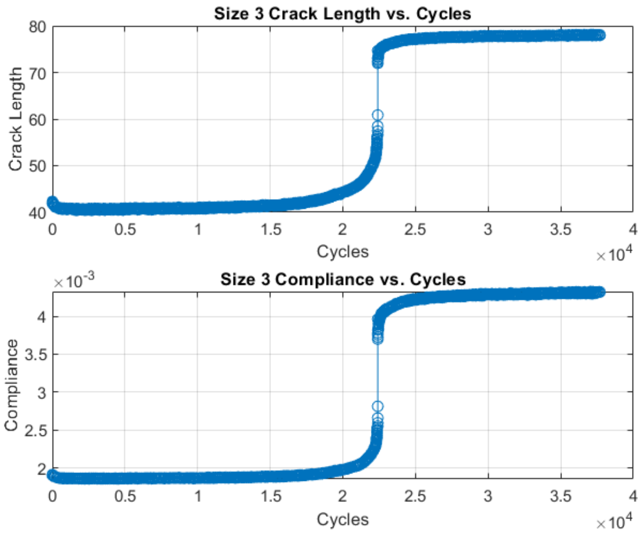

Fig. 21 Size 3 Compliance Calibration Linear Regression

Finally using the linear regression for compliance in Equation 7, the energy release rate can be shown as

$$G_{IImax} = \frac{3mP_{max}^2 a^2}{2b} \tag{19}$$

Using the values from the compliance tests, this can then be substituted back into Equation 11 to get

$$K_{IImax} = \sqrt{\frac{3mP_{max}^2 a^2 L^3}{8Abh^3}} \tag{20}$$

Where according to ASTM D-7905, the value of E can be calculated as

$$E = \frac{L^3}{4Abh^3} \tag{21}$$

From this, ΔK can be calculated as the difference between the maximum and minimum stress intensity factor, found at the peaks of the sinusoidal loading condition.

$$\Delta K = K_{IImax} - K_{IImin} \tag{22}$$

Now that both aspects of the Paris curve have been calculated, the values of $\frac{\mathrm{d}a}{\mathrm{d}N}$ can be plotted against the values of ΔK. These results can be found in Figure 23

Looking closely at the crack propagation data of the three sizes, the slopes of each Paris-Erdogan curve, m = 13.8, 17.8, and 17.5, can be used to describe the crack growth behavior of different sizes of carbon/epoxy beams. The slope

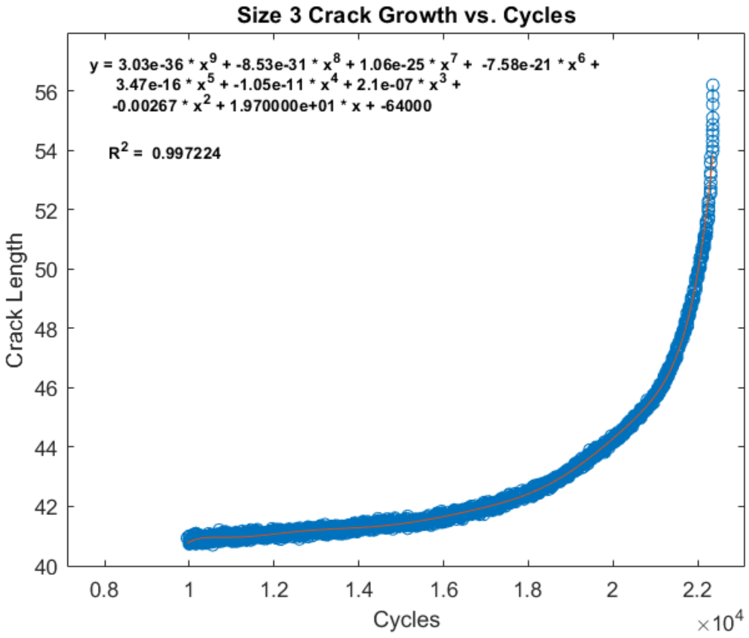

Fig. 22 Size 3 Crack Growth Polynomial Fit Equation

calculated was based on an average value of the linear region for all the specimen sizes with at least three samples for each specimen size. The Paris-Erdogan curves show nearly no difference on the slopes for sizes 2 and 3, but the slope is very different for the size 1 specimen. It has a slope m = 13.8 for the size 1, while the larger specimen sizes 2 and 3 have a steeper slope of m = 17.8 and 17.7, respectively.

Looking more closely at the threshold ΔK values, we can see in Figure 24 that the values of the threshold also change with the specimen size. These threshold values were obtained by taking an average of all the data points within the threshold region. Error bars representing one standard deviation away from the mean were also added to show the uncertainty behind these measurements. Due to the data variance of the size 2 specimens, the resulting had a much larger error.

3.2.3. Size Effect Law for Fatigue

However, since the results of this LEFM analysis show that the threshold values are dependant on specimen size, this contradicts the idea the the ΔK_{th} should be a singular value to be a material property. This again reiterates that LEFM does not apply fully to quasibrittle size affected materials. For these reasons, the size of the FPZ must be taken into account by applying Bažant's Type II Size Effect Law[19]. This method has been shown in the literature to successfully characterize fracture properties of various quasibrittle materials (e.g., concrete, ceramics, rocks, sea ice, fiber-reinforced polymers, wood, bone, nacre, etc.) [12, 13]. This research follows the method done by Qiao et al. used for mode I fracture and fatigue[21]. For fatigue, the equation to calculate the energy amplitude of fatigue initiation can be seen in

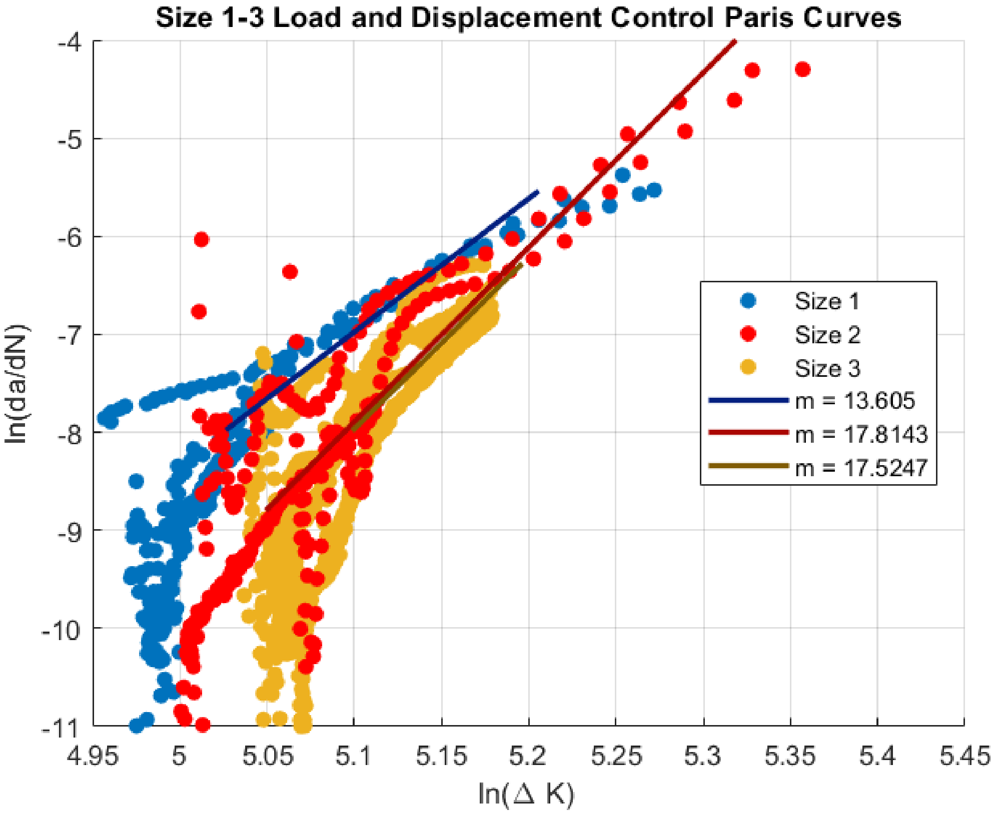

Fig. 23 Size 1-3 Paris Curve with Slope Values

Equation23

$$\Delta G_{th}(\alpha_{eq}) = \Delta G_{th}(\alpha_0 + \frac{c_{f,c}}{D}) \approx \frac{\left(\sigma_{n,max}^2 - \sigma_{n,min}^2\right) D}{E} \left[g(\alpha_0) + \frac{c_{f,c}}{D} g'(\alpha_0)\right] \tag{23}$$

where $\Delta G_{th} = \Delta G_{max} - \Delta G_{min}$, $\alpha_0 = \frac{a_0}{D}$ is the normalized initial crack length, $\alpha_{eq} = \alpha_0 + \frac{c_{f,c}}{D}$ is the effective crack length, $c_{f,c}$ is the effective FPZ, E is the elastic modulus, D is the scaled thickness of the specimens, and $g(\alpha_0)$ is the dimensionless energy release rate. It's important to note that Equation23 will only describe the fatigue condition if the first derivative of $g(\alpha_0)$, $g'(\alpha_0)$, is greater than 0. This indicates that the structure has a positive geometry. $\sigma_{n,max}$ and $\sigma_{n,min}$ are the nominal stresses. For this research, the nominal stress is defined in all cases as $\sigma_n = \frac{P}{Bh}$, calculated by the maximum and minimum loads from the peak and trough of an applied load. By introducing a value known as the stress ratio $R = \frac{\sigma_{n,min}}{\sigma_{n,max}}$, the previous Equation 23 can now be simplified to

$$\Delta G_{th}(\alpha_0 + \frac{c_{f,c}}{D}) \approx \frac{R^* \left(\Delta\sigma_{n,th}\right)^2 D}{E} \left[g(\alpha_0) + \frac{c_{f,c}}{D} g'(\alpha_0)\right] \tag{24}$$

where $R^* = \frac{1+R}{1-R}$, and $\Delta\sigma_{n,th} = \sigma_{n,max} - \sigma_{n,min}$ is the nominal stress amplitude.

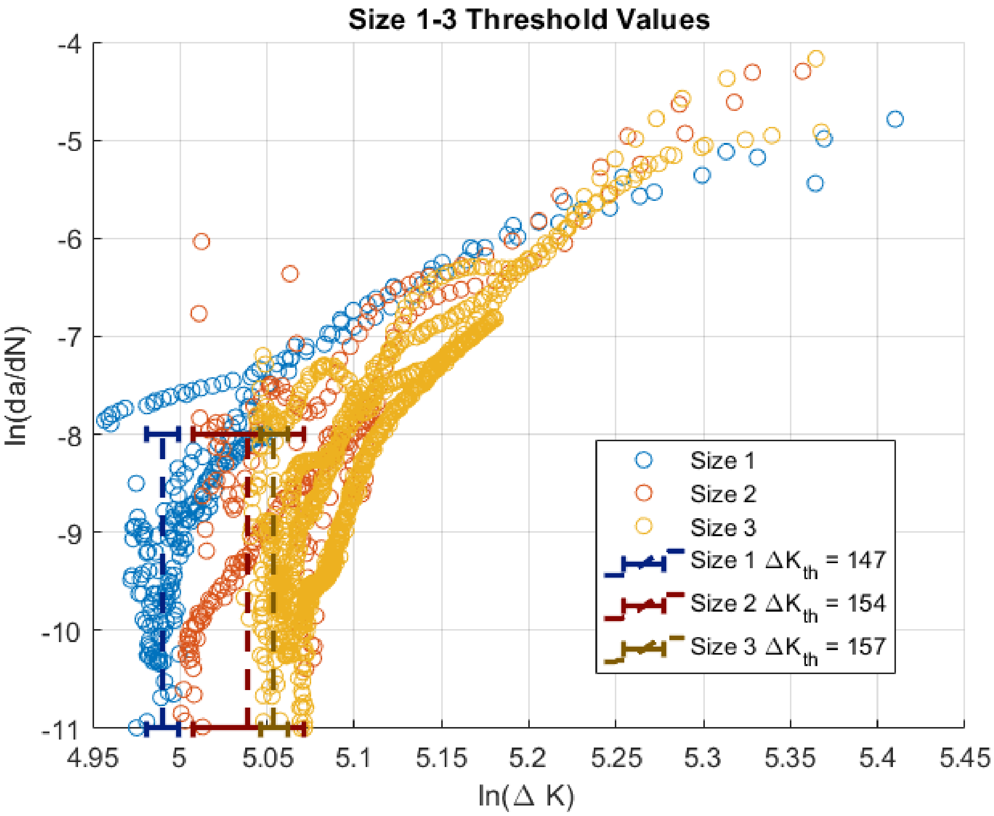

Fig. 24 Size 1-3 Paris Curve with Threshold Values

In order to calculate the values of $g(\alpha_0)$ and $g'(\alpha_0)$, our experimental results can be enhanced with the integration of Finite Element Analysis (FEA). FEA can be used to find the J-integral, which will then be used to determine the energy release rate of the material. For the modeling aspect, ABAQUS explicit was used, employing quarter quadratic elements, to model the size 1 specimens. The ENF beam model was configured with a designated crack tip and crack seam. It should be noted that for the simulation of the crack seam, a frictionless surface to surface contact was used to simulate the phenomena occurring at the crack surfaces. A frictionless case was used since it was previously confirmed that the energy dissipated by friction does not have negligible effect on the calculation of the energy release rate[19]. Similar to the experimental 3-point bending tests, an applied load was simulated at the midpoint of the beam, which had simply supported boundary conditions at the ends of the beam. A refined mesh of around 32000 elements were used, with most of the elements being centered around the crack tip, as can be seen in Figure 25. From this model, the J-integral around the crack tip was calculated and the following expression was used to calculate the dimensionless energy release rate $g(\alpha_0)$[24].

$$g(\alpha) = \frac{G(\alpha)E}{D\sigma_n^2} \tag{25}$$

From this, in order to calculate $g'(\alpha)$, two other normalized crack lengths which are close to the original value of α, in

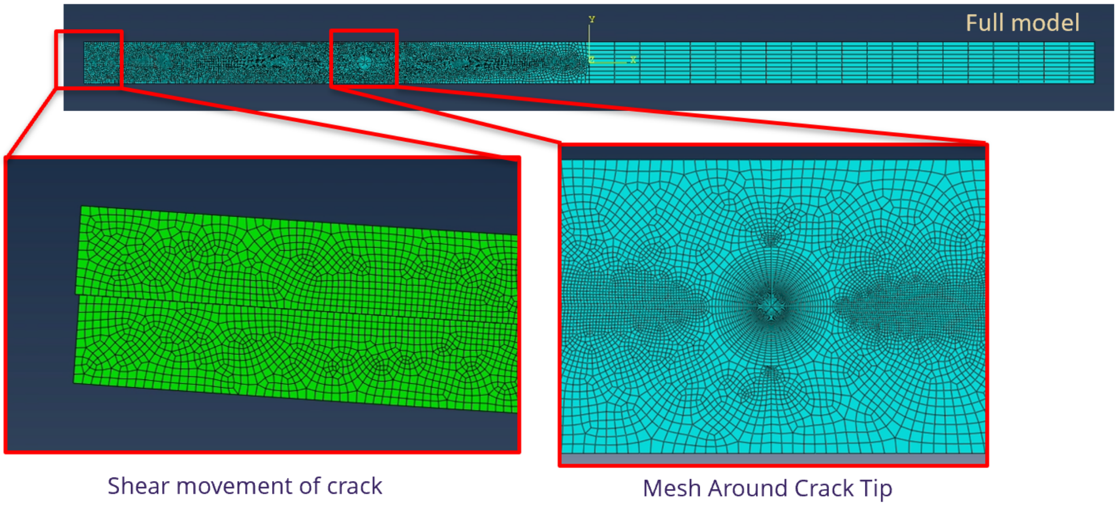

Fig. 25 ABAQUS model, highlighting shear movement and mesh refinement

this case 9.5 mm, 10 mm, and 10.5 mm, were used to perform a linear regression of the dimensionless energy release rate, this can be seen in Figure 26, where the value of $g'(\alpha)$ is the slope of the linear regression. Using this method, the values of the dimensionless energy release rate and its derivative were found to be $g(\alpha_0) = 198.2$ and $g'(\alpha_0) = 52.14$, where $\alpha_0 = \frac{a_0}{D} = 7.11$.

Now, to obtain the values of ΔG_{th} and $c_{f,c}$, Equation 23 can be rearranged into the following equation to fit the experimental data into an expression used for a linear regression analysis.

$$\frac{1}{R^* \left(\Delta\sigma_{n,th}\right)^2 g'(\alpha_0)} = \frac{g(\alpha_0)D}{g'(\alpha_0)\Delta G_{th}E} + \frac{c_{f,c}}{\Delta G_{th}E} \tag{26}$$

This size effect regression takes a linear form as seen below to calculate our size effect parameters A and C

$$Y = Ax + C \tag{27}$$

Applying this to Equation 26 gives

$$Y = \frac{1}{\Delta G_{th}E}X + \frac{c_{f,c}}{\Delta G_{th}E} \tag{28}$$

Where $Y = \frac{1}{R^*\left(\Delta\sigma_{n,th}\right)^2 g'(\alpha_0)}$ and $X = \frac{g(\alpha_0)D}{g'(\alpha_0)}$. The results of this linear regression analysis can be seen in Figure 27, where $A = 1.81E-5$ and $C = 1.22E-4$. Now, the fracture energy and the size of the FPZ can be calculated using the relationships for the size effect parameters in Equations 29 and 30

$$A = \frac{1}{\Delta G_{th}E} \tag{29}$$

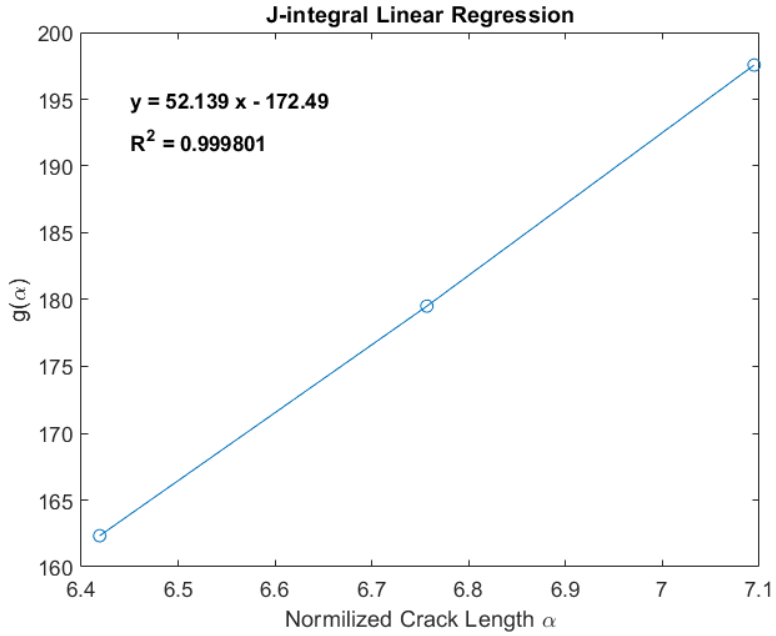

Fig. 26 Linear regression of J-Integral Abaqus values

$$C = \frac{c_{f,c}}{\Delta G_{th} E} \tag{30}$$

With this information, the size effect curve can now be plotted. Equation 24 can be rearranged according to Bažant's type II size effect law as seen in Equation 1

$$\Delta\sigma_{n,th} = \frac{\Delta\sigma_{0,c}}{\sqrt{1 + \frac{D}{D_{0,c}}}} = \sqrt{\frac{\Delta G_{th}(\alpha_{eq})E}{\left[\left(Dg(\alpha_0) + c_{f,c}g'(\alpha_0)\right) R^*\right]}} \tag{31}$$

Where $\Delta\sigma_{0,c} = \frac{\Delta G_{th}(\alpha_{eq})E}{\left[c_{f,c}g'(\alpha_0)R^*\right]}$ and $D_{0,c} = \frac{c_{f,c}g'(\alpha_0)}{g(\alpha_0)}$. It is possible that the normalized initial crack lengths for different specimens and sizes are not the same for every specimen. In this case, the following equation can be used to adjust the experimental data to an ideal case. By assuming that specimens of differing crack lengths have the same ΔG_{th},

$$\frac{\Delta\sigma^2_{n,th,experiment}D}{E}\left[g(\alpha_{0,experiment}) + \frac{c_{f,c}}{D}g'(\alpha_{0,experiment})\right] = \frac{\Delta\sigma^2_{n,th,ideal}D}{E}\left[g(\alpha_{0,ideal}) + \frac{c_{f,c}}{D}g'(\alpha_{0,ideal})\right] \tag{32}$$

Equation 32 can be rearranged to then solve for the ideal nominal stress amplitude

$$\Delta\sigma_{n,th,ideal} = \Delta\sigma_{n,th,exp}\sqrt{\frac{\left[Dg(\alpha_{0,exp}) + c_{f,c}g'(\alpha_{0,exp})\right]}{\left[Dg(\alpha_{0,ideal}) + c_{f,c}g'(\alpha_{0,ideal})\right]}} \tag{33}$$

By applying Equation 33 to the experimental data, the final results and the fitting to the Size Effect Law can be seen in Figure 28 In this plot, the nominal stress amplitude, $\Delta\sigma_{n,th}\sqrt{R^*}$, which is normalized by $\sqrt{R^*}$ for ease of calculation, is

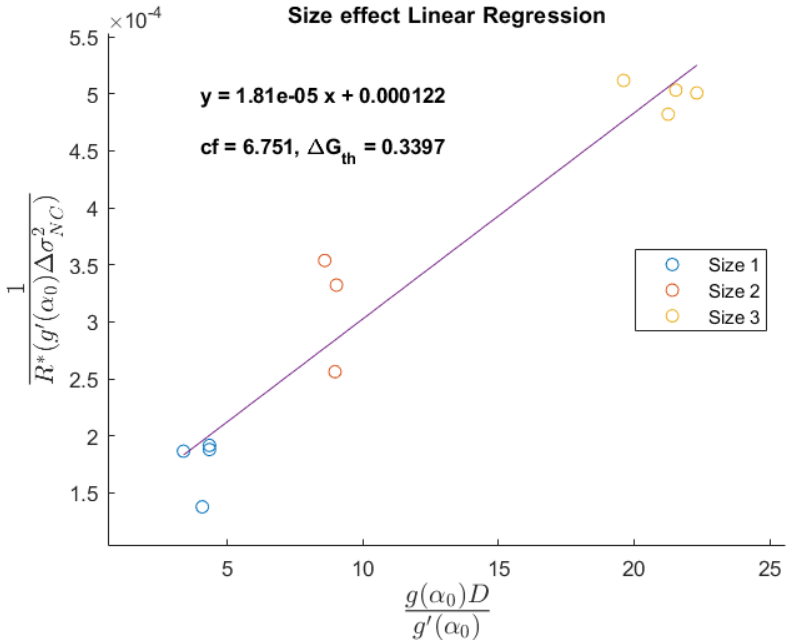

Fig. 27 Linear Regression to Characterize Size Effect Parameters

plotted as a function of the scaled specimen thickness D in a double natural logarithmic scale. As can be seen in 28, the experimental data are an excellent fit to the size effect. This shows that for a sufficiently large specimen, the fatigue crack propagation can be properly characterized by LEFM. However, this is not the case for smaller specimens, such as the size 1 case. In 28, for a smaller specimen size, the value of $\Delta\sigma_{n,th}\sqrt{R^*}$ deviates from the LEFM values, denoted by the green dashed line. This curve properly incorporates the FPZ that occurs at the fracture front for this quasibrittle material. From Equations 29 and 30, it was found that $\Delta G_{th} = 0.340$ N/mm and $c_{f,c} = 6.75$ mm. Then by applying Equation 34

$$\Delta K_{th} = \sqrt{\Delta G_{th} E^*} \tag{34}$$

Where E^* is the effective elastic modulus. This value of this is shown in Equation 35.

$$E^* = \sqrt{\frac{2E_1E_2\sqrt{\lambda}}{1+\rho}} \tag{35}$$

Where $\lambda = \frac{E_2}{E_1}$ and $\rho = \frac{\sqrt{E_1E_2}}{2G_{12}} - \sqrt{\nu_{12}\nu_{21}}$. The values of E_1, E_2. G_{12}, ν_{12}, and ν_{21} are in plane elastic constants of the composite material. The stress intensity factor threshold was found to be $\Delta K_{th} = 203.0\ \mathrm{MPa}\sqrt{\mathrm{mm}}$. Its worth highlighting again that using traditional LEFM to calculated the stress intensity factor would lead to size affected values. Using LEFM presents a major contradiction to the idea of the ΔK_{th} being a material property. Table 5 shows the difference between the ΔK_{th} calculated using LEFM and the percent deviation from the actual value provided by the

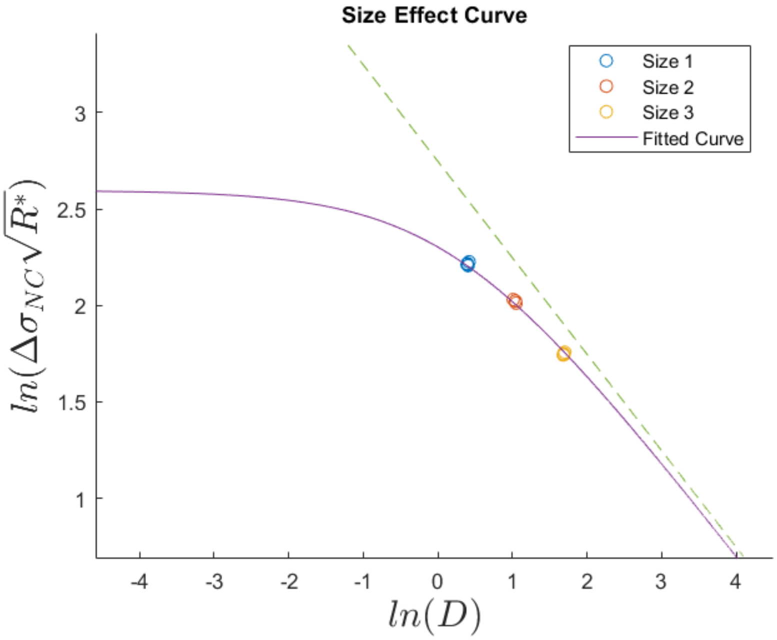

Fig. 28 Linear Regression to Characterize Size Effect Parameters

size effect law.

Specimen Size	ΔK_{th}(MPa$\sqrt{\text{mm}}$)	% Deviation
Size 1	147.0	27.61%
Size 2	154.3	23.99%
Size 3	157.1	22.61%

Table 5 ΔK_{th} Calculated Using LEFM

4. Conclusion

This research investigated the size effect on the mechanical behaviors and damage characteristics of carbon/epoxy polymer composites in a cyclic fatigue loading conditions in mode II conditions. These results highlighted the following conclusions.

1) The Paris-Erdogan curves for carbon/epoxy beams were constructed using the compliance to measure the crack length showed that there was a noticeable effect from the specimen size. Both the values of the fatigue threshold as well as the crack propagation rate were smaller for the smaller specimen sizes. This contradicts the idea that the Paris-Erdogan curve is a material property. This is likely due to how the original Paris-Erdogan curve was based on the LEFM assumption. This shows that the Paris-Erdogan curve cannot be applied like traditional materials and must be properly scaled before use on carbon/epoxy structures.
2) Analysis of the scaling fatigue behavior was done by calculating the ΔK_{th} for each specimen. However, it was found that using LEFM to calculate the fatigue threshold stress intensity factor amplitude results in a ΔK_{th} that

depends on specimen size. The stress intensity factors from LEFM were 147.0 MPa$\sqrt{\text{mm}}$, 154.3 MPa$\sqrt{\text{mm}}$, and 157.1 MPa$\sqrt{\text{mm}}$ for the size 1, 2 and 3 specimens respectively.

3) The effects of the FPZ size on specimens was able to be characterized by applying Bažant's Type II Size Effect Law. The experimental nominal stress amplitude data showed an excellent fit with the size effect law. The threshold stress intensity factor amplitude was also able to be defined as a material propriety, as $\Delta K_{th} = 203.0\text{MPa}\sqrt{\text{mm}}$. The difference between the LEFM and the size effect law results was very significant. It was found that the values calculated by LEFM were 27.61%, 23.99%, and 22.61% smaller than the size effect law values for size 1, 2 and 3 specimens respectively. This deviation is more pronounced in smaller specimen sizes, with the deviation tending to zero with sufficient specimen size, where the FPZ size becomes negligible compared to the size of the specimens. This further highlights the importance of accounting for the FPZ in smaller quasibrittle structures, such as the carbon/epoxy beams shown here.

References

[1] Kim, H.-G., and Wiebe, R., "Numerical investigation of stress states in buckled laminated composite plates under dynamic loading," *Composite Structures*, Vol. 235, 2020, p. 111743.

[2] Bažant, Z., Gettu, R., Jirásek, M., Barr, B., Carol, I., Carpinteri, A., Elices, M., Huet, C., Mihashi, H., Nemati, K., Planas, J., Ulm, F.-J., Mier, J., Vliet, M., Burtscher, S., Chiaia, B., Dempsey, J., Ferro, G., Gopalaratnam, V., and Willam, K., "RILEM TC QFS Quasibrittle fracture scaling and size effect- Final report," *Materials and Structures/Materiaux et Constructions*, Vol. 37, 2004, pp. 547–568. https://doi.org/10.1617/14109.

[3] Shivakumar, K. N., Panduranga, R., Skujins, J., and Miller, S., "Assessment of mode-II fracture tests for unidirectional fiber reinforced composite laminates," *Journal of Reinforced Plastics and Composites*, Vol. 34, No. 23, 2015, pp. 1905–1925.

[4] Howe, R., "Experimental Investigation of Mode II Fracture and Fatigue in Unidirectional Carbon/Epoxy Composite Beams," 2021.

[5] Kaw, A., *Mechanics of Composite Materials*, Mechanical and Aerospace Engineering Series, CRC Press, 2005. URL https://books.google.com/books?id=MwHLBQAAQBAJ.

[6] Foreman, C., *Advanced Composites*, Jeppesen Sanderson, 2002. URL https://books.google.com/books?id=N9S3AAAACAAJ.

[7] Sloan, J., "Composites World: Skinning the F-35 Fighter," , 2009. URL https://www.compositesworld.com/articles/skinning-the-f-35-fighter.

[8] Boeing, "Boeing 787 By Design," , 2020. URL https://www.boeing.com/commercial/787/by-design/#/featured.

[9] Knight, D., Chazot, O., Austin, J., Badr, M. A., Candler, G., Celik, B., de Rosa, D., Donelli, R., Komives, J., Lani, A., Levin, D., Nompelis, I., Panesi, M., Pezzella, G., Reimann, B., Tumuklu, O., and Yuceil, K., "Assessment of predictive capabilities for aerodynamic heating in hypersonic flow," *Progress in Aerospace Sciences*, Vol. 90, 2017, pp. 39–53.

[10] Asp, L. E., Sjögren, A., and Greenhalgh, E. S., "Delamination growth and thresholds in a carbon/epoxy composite under fatigue loading," *Composites Technology and Research*, Vol. 23, No. 2, 2001, pp. 55–68.

[11] Loukil, M., "Experimental and Numeriacal Studies of Intralaminar Cracking in High Performance Composites," Ph.D. thesis, 10 2013.

[12] Bazant, Z., and Planas, J., *Fracture and Size Effect in Concrete and Other Quasibrittle Materials*, 2019. https://doi.org/10.1201/9780203756799.

[13] Bažant, Z. P., Le, J.-L., and Salviato, M., *Quasibrittle Fracture Mechanics and Size Effect: A First Course*, Oxford University Press, 2021.

[14] Park, K., and Paulino, G., "Cohesive Zone Models: A Critical Review of Traction-Separation Relationships Across Fracture Surfaces," *Applied Mechanics Reviews*, Vol. 64, 2011, pp. 1002–. https://doi.org/10.1115/1.4023110.

[15] Paris, P. C., “A rational analytic theory of fatigue,” 1961. URL https://api.semanticscholar.org/CorpusID:135979378.

[16] Paris, P. C., and Erdogan, F., “A Critical Analysis of Crack Propagation Laws,” *Journal of Basic Engineering*, Vol. 85, 1963, pp. 528–533. URL https://api.semanticscholar.org/CorpusID:136607277.

[17] Pugno, N., Ciavarella, M., Cornetti, P., and Carpinteri, A., “A generalized Paris’ law for fatigue crack growth,” *Journal of the Mechanics and Physics of Solids*, Vol. 54, No. 7, 2006, pp. 1333–1349. https://doi.org/https://doi.org/10.1016/j.jmps.2006.01.007, URL https://www.sciencedirect.com/science/article/pii/S0022509606000196.

[18] ASTM International, “D7905: Standard Test Method for Determination of the Mode II Interlaminar Fracture Toughness of Unidirectional Fiber-Reinforced Polymer Matrix Composites,” 2014.

[19] Salviato, M., Kirane, K., Bažant, Z. P., and Cusatis, G., “Mode I and II Interlaminar Fracture in Laminated Composites: A Size Effect Study,” *Journal of Applied Mechanics*, Vol. 86, No. 9, 2019, p. 091008.

[20] Guo, K. D., Qiao, Y., and Salviato, M., “Scaling of Fatigue Crack Growth in Pristine Epoxy,” *American Society for Composites 2018*, 2018. URL https://api.semanticscholar.org/CorpusID:139324592.

[21] Qiao, Y., Guo, K., and Salviato, M., “Size Effect and Scaling in Quasi-static and Fatigue Fracture of Graphene Polymer Nanocomposites,” *Polymer Composites*, 2023. https://doi.org/10.1002/pc.27424.

[22] ASTM International, “D7905: Standard Guide for Preparation of Flat Composite Panels with Processing Guidelines for Specimen Preparation,” 2015.

[23] Al-Khudairi, O., Hadavinia, H., Waggott, A., Lewis, E., and Little, C., “Characterising mode I/mode II fatigue delamination growth in unidirectional fibre reinforced polymer laminates,” *Materials & Design (1980-2015)*, Vol. 66, 2015, pp. 93–102. https://doi.org/https://doi.org/10.1016/j.matdes.2014.10.038, URL https://www.sciencedirect.com/science/article/pii/S0261306914008267.

[24] Rice, J., “A Path Integral and the Approximate Analysis of Strain Concentration by Notches and Cracks,” *Journal of Applied Mechanics*, Vol. 35, 1968, pp. 379–386. https://doi.org/10.1115/1.3601206.